Optimal experimental design for nano-particle atom-counting from high-resolution STEM images

Reference:

de Backer Annick, De wael A., Gonnissen Julie, Van Aert Sandra.- Optimal experimental design for nano-particle atom-counting from high-resolution STEM images

Ultramicroscopy - ISSN 0304-3991 - 151(2015), p. 46-55

DOI: http://dx.doi.org/doi:10.1016/j.ultramic.2014.10.015

Optimal experimental design for nano-particle atom-counting from high-resolution STEM images

A. De Backer[a], A. De wael[a], J. Gonnissen[a], S. Van Aert[a,1,*]

[a]*Electron Microscopy for Materials Science (EMAT), University of Antwerp, Groenenborgerlaan 171, B-2020 Antwerp, Belgium*

Abstract

In the present paper, the principles of detection theory are used to quantify the probability of error for atom-counting from high resolution scanning transmission electron microscopy (HR STEM) images. Binary and multiple hypothesis testing have been investigated in order to determine the limits to the precision with which the number of atoms in a projected atomic column can be estimated. The probability of error has been calculated when using STEM images, scattering cross-sections or peak intensities as a criterion to count atoms. Based on this analysis, we conclude that scattering cross-sections perform almost equally well as images and perform better than peak intensities. Furthermore, the optimal STEM detector design can be derived for atom-counting using the expression for the probability of error. We show that for very thin objects LAADF is optimal and that for thicker objects the optimal inner detector angle increases.

Keywords: High-resolution scanning transmission electron microscopy (HR

*Corresponding author

Email address: sandra.vanaert@uantwerpen.be (S. Van Aert)

[1]*Phone*: +32 3 2653252

[2]Fax: +32 3 2653318

STEM), Electron microscope design and characterisation, Data processing/image processing

1. Introduction

Ever since its invention in 1931, the optical capabilities of the electron microscope have always been restricted by effects of inherent lens aberrations, preventing its spatial resolution to reach values near the theoretical limit. Since electron microscopy plays an important role in progressing current science and technology, exceptional efforts were made to overcome these restraints. However, only in 1990, aberration-corrected electron optics was developed for the first time, when the three Wolf Prize Laureates at the time worked together. Their research leading to the achieved result was based on a new optical concept for the spherical aberration correction of the objective lens in the electron microscope, which was invented by Harald Rose [1, 2]. As a result of the introduction of aberration-corrected electron microscopes the interpretability of the images has recently improved down to atomic resolution [3, 4]. At the same time other instrumental developments have improved the resolution of electron microscopes, such as the invention of the monochromator [5]. In addition, electron microscopists nowadays can choose between an increasing versatility of microscope settings. One can for example choose between TEM or STEM, between imaging or diffraction techniques, and between a wide range of different detectors, from which several types were proposed and investigated by Harold Rose like the ABF STEM detector [6]. Furthermore, an electron microscopist can tune parameters such as defocus, accelerating voltage, spherical aberration, energy spread of

incoming electrons, beam tilt and crystal tilt. A better resolution can therefore be achieved by tuning these parameters. A resolution beyond 1 $\mathring{A}$ allows microscopists to visually distinguish atom columns of solids oriented along a main zone axis. One can now not only interpret STEM images qualitatively in terms of resolution, but also quantitatively in terms of precision [7–10]. Unlike qualitative materials characterisation methods, which are based on a visual interpretation of the observations, quantitative methods allow the extraction of local structure information at the subangstrom level. This helps to obtain a precision of the order of $0.01 - 0.1$ $\mathring{A}$ for the atomic column positions [11, 12]. In order to achieve the highest possible precision with which unknown structure parameters can be determined, the question rises which microscope settings are optimal. It is of great importance to be able to specify structure parameters such as the number of atoms in a column, the atomic number Z and the positions of the atoms, with the highest possible precision, since the physical behaviour and properties of crystalline nano-particles are determined by their exact structural and chemical composition.

Until now, different methods have been proposed and investigated to count the number of atoms of a crystalline nano-structure from HAADF STEM images. As a first attempt to solve the counting problem, Erni et al. [13] proposed to measure the absolute value of the intensity differences between neighbouring atom columns. LeBeau et al. [14–18] compared simulated atom column intensities with normalised experimentally measured atom column intensities in order to count the number of atoms. Van Aert et al. [19] developed a new quantitative, statistical model-based method to count the number of atoms from HAADF STEM images of a structure viewed along

a zone-axis. This approach may help determine the three-dimensional (3D) arrangement of atoms in crystalline nano-particles [20–22]. Indeed, by applying this statistical counting method and combining the results for different viewing directions, the 3D atomic structure can be attained using discrete tomography [23, 24]. Moreover, single atom sensitivity is shown to be feasible in practice using this statistical model-based method, when taking aspects into consideration that affect the accuracy and precision with which the atoms in a column can be estimated, such as the number of atom columns available in the observed STEM image, the number of columns having a different number of atoms, and the amount of noise [19, 25].

In the present work we will explore the theoretical limits to the precision with which the number of atoms in a column can be estimated from HR STEM images. Therefore, STEM images are interpreted quantitatively and the optimal experiment design to count the number of atoms in a column is investigated. So far, the so-called Cramér-Rao lower bound (CRLB) has been proven to be an optimal tool to determine a theoretical lower bound on the precision with which continuous parameters such as atomic column positions and intensities can be estimated [7–9, 26–38]. However, this lower bound can only be derived for continuous parameters. Therefore an alternative measure using the principles of detection theory is introduced in [36, 39] for problems concerning the estimation of the atomic number, which is a discrete parameter. This measure will here be extended to the atom-counting problem, where the number of atoms in a column can also be considered as a discrete parameter.

Statistical detection theory allows us to derive a criterion to describe the

performance of atom-counting provided that the expectations as well as statistical fluctuations of the experimental images can be accurately modelled. In this framework, the atom-counting problem is formulated as a statistical hypothesis test, where each hypothesis corresponds to a specific number of atoms in an atomic column. The optimality criterion can then be defined as the probability to choose the wrong hypothesis, i.e. the so-called probability of error. In order to compute this probability of error, use can be made of realistic simulations to describe the experimental images [15, 19, 40–42], and knowledge about the statistics of the image pixel values. Ultimately, the image pixel values will be Poisson distributed because of the unavoidable presence of counting noise. This inherent presence of statistical fluctuations will therefore set fundamental limits to the precision with which the number of atoms can be determined.

By minimising the expression for the probability of error, the optimal experiment design can be derived. In this paper the optimal inner and outer angle of an annular STEM detector will be computed. So far the HAADF STEM detector is often used for atom-counting [13, 14, 19–22, 43–46]. Here it will be investigated if this imaging mode remains optimal in terms of atom-counting precision. This procedure to derive the optimal STEM detector can then be applied in practical future research problems so as to further improve the precision to count atoms in a column [47].

The organisation of the paper is as follows. In section 2, detection theory is discussed and the probability of error is derived for both a binary and a multiple hypothesis test. In section 3, the proposed method will be applied to a simulation of a $SrTiO_3$ crystal to derive optimal inner and outer angles

of the annular STEM detector. This will be done for a binary as well as for a multiple hypothesis test. In Section 4, the results found for the binary hypothesis test will be discussed and compared to those for the multiple hypothesis test. In Section 5, conclusions are drawn.

2. Detection theory

When one is considering the problem of counting the number of atoms in a projected atomic column of a mono-type crystalline structure from HR STEM images, the goal is to obtain the number of atoms in a column as precisely as possible. In this section, an expression for the probability to miscount the number of atoms, the so-called probability of error, will be derived. To start simple we use a binary hypothesis test in which only two possible successive numbers of atoms are considered as possible outcomes. Next, this theory will be extended toward a multiple hypothesis test. In that case, all possible hypotheses up to a certain thickness for the column have to be included.

2.1. Binary hypothesis test for atom-counting

In the case where one wants to know if there are n or $n+1$ atoms in a projected atomic column, the hypotheses are given by:

$$\begin{aligned} \mathcal{H}_0 &: n_{\mathcal{H}_0} = n \\ \mathcal{H}_1 &: n_{\mathcal{H}_1} = n_{\mathcal{H}_0} + 1 \end{aligned} \tag{1}$$

where $\mathcal{H}_0$ is referred to as the null hypothesis, $\mathcal{H}_1$ as the alternative hypothesis and $n_{\mathcal{H}_i}$ denotes the number of atoms under hypothesis $\mathcal{H}_i$. In order

to express a prior belief in the likelihood of the hypotheses, we assume that the prior probabilities $P(\mathcal{H}_0)$ and $P(\mathcal{H}_1)$ associated with these hypotheses are known. It is reasonable to assign equal prior probabilities of 1/2 if both hypotheses are equally likely. Throughout the paper, we will always assume that both hypotheses are equally likely. If we follow the quantitative method proposed in [36], the goal is now to quantify the probability of assigning the wrong hypothesis. In a so-called Bayesian approach, this probability of error $\mathrm{P_e}$ is defined as:

$$\begin{aligned} \mathrm{P_e} &= \Pr\{\text{decide } \mathcal{H}_0, \mathcal{H}_1 \text{ true}\} \\ &\quad + \Pr\{\text{decide } \mathcal{H}_1, \mathcal{H}_0 \text{ true}\} \\ &= P(\mathcal{H}_0|\mathcal{H}_1)\,P(\mathcal{H}_1) + P(\mathcal{H}_1|\mathcal{H}_0)\,P(\mathcal{H}_0) \end{aligned} \tag{2}$$

where $P(\mathcal{H}_i|\mathcal{H}_j)$ is the conditional probability of deciding $\mathcal{H}_i$ when $\mathcal{H}_j$ is true. Using criterion (2), the two possible errors are weighted appropriately to yield an overall error measure. Decision rules are now defined such that the probability of error is minimised. For this purpose, it is shown in [48] that we should then decide $\mathcal{H}_1$ if

$$\frac{p(\omega;\mathcal{H}_1)}{p(\omega;\mathcal{H}_0)} > \frac{P(\mathcal{H}_0)}{P(\mathcal{H}_1)} = \gamma = 1, \tag{3}$$

otherwise $\mathcal{H}_0$ is decided. In this expression, $p(\omega;\mathcal{H}_i)$ is the conditional probability function assuming $\mathcal{H}_i$ to be true, for the stochastic variable ω. The exact expression for this probability function will be discussed for three different measures that can be used as a criterion to count atoms in a projected atomic column: peak intensities (PI), scattering cross-sections (CS), HR STEM image pixel values of a projected atomic column. The stochastic

variable ω will take a different form for these three measures:

$$\omega^{PI} \qquad \text{for peak intensities} \tag{4}$$

$$\omega^{CS} = \sum_{k=1}^{K}\sum_{l=1}^{L} \omega_{kl} \cdot dx^2 \qquad \text{for cross-sections} \tag{5}$$

$$\boldsymbol{\omega}^{Im} = [\omega_{11}, \omega_{12}, \omega_{21}, ..., \omega_{KL}]^T \text{for images} \tag{6}$$

where the parameter ω_{kl} corresponds to the random variables describing the pixel intensities of the STEM image of the atomic column and ω^{PI} corresponds to the random variable describing the pixel intensity at the position of the atomic column. The index kl denotes the probe position $(x_k, y_l)^T$ for a set of KL pixel observations, and dx denotes the pixel size of the STEM image.

2.2. Peak intensities (PI)

When assuming that the pixels in a STEM image are statistically independent electron counting results, which are modelled as a Poisson distribution, the conditional probability function for the pixel intensity at the position of a projected atomic column is given by:

$$p(\omega^{PI}; \mathcal{H}_i) = \frac{\left(\lambda^{PI}_{\mathcal{H}_i}\right)^{\omega^{PI}}}{\omega^{PI}!} \exp\left(-\lambda^{PI}_{\mathcal{H}_i}\right), \tag{7}$$

where the parameter $\lambda^{PI}_{\mathcal{H}_i} = \mathbb{E}_{\mathcal{H}_i}\left[\omega^{PI}\right]$ corresponds to the expectation value for the pixel intensity of the STEM image at the position of the projected atomic column. Since this expectation value will depend on which hypothesis $\mathcal{H}_i$ is assumed to be true, also the probability function depends on $\mathcal{H}_i$. In general, this expectation value can be computed under each hypothesis using

software that allows one to simulate a STEM image for a given input material's structure and a given set of microscope parameters [42]. Following the decision rule of Eq. (3), for equal prior probabilities $P(\mathcal{H}_0) = P(\mathcal{H}_1) = 1/2$, we decide $\mathcal{H}_1$ if:

$$p(\omega^{PI}; \mathcal{H}_1) > p(\omega^{PI}; \mathcal{H}_0) \tag{8}$$

otherwise $\mathcal{H}_0$ is decided. An illustration of the conditional probability functions $p(\omega^{PI}; \mathcal{H}_i)$ of Eq. (7) for both hypotheses is given in Fig. 1(a) for the peak intensities of a Sr column consisting of either 15 or 16 atoms. The dark grey region denotes the error which is made if $\mathcal{H}_0$ is chosen while $\mathcal{H}_1$ is correct, and vice versa for the light grey region. It is clear from this image that the probability of error then corresponds to the overlapping area of the two conditional probability functions $p(\omega^{PI}; \mathcal{H}_0)$ and $p(\omega^{PI}; \mathcal{H}_1)$. This probability can analytically be computed using the cumulative distribution function of the Poisson distribution:

$$\begin{aligned} P_e =& \frac{1}{2} P(\mathcal{H}_0|\mathcal{H}_1) + \frac{1}{2} P(\mathcal{H}_1|\mathcal{H}_0) \\ =& \frac{1}{2} F\left(x^{PI}; \lambda^{PI}_{\mathcal{H}_1}\right) + \frac{1}{2}\left[1 - F\left(x^{PI}; \lambda^{PI}_{\mathcal{H}_0}\right)\right] \end{aligned} \tag{9}$$

where $F\left(x^{PI}; \lambda^{PI}_{\mathcal{H}_i}\right)$ equals the Poisson cumulative distribution function with parameter $\lambda^{PI}_{\mathcal{H}_i}$ evaluated at the value x^{PI}, with x^{PI} the intersection between the two conditional distribution functions $p(\omega^{PI}; \mathcal{H}_0)$ and $p(\omega^{PI}; \mathcal{H}_1)$ given by:

$$x^{PI} = \frac{\lambda^{PI}_{\mathcal{H}_0} - \lambda^{PI}_{\mathcal{H}_1}}{\ln \frac{\lambda^{PI}_{\mathcal{H}_0}}{\lambda^{PI}_{\mathcal{H}_1}}}. \tag{10}$$

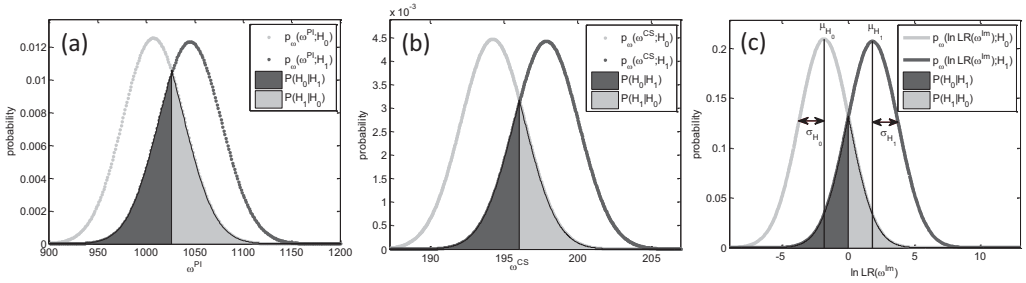

Figure 1: Calculation of the probability of error for a binary hypothesis test for (a) peak intensities ω^{PI} ($D = 10^6$ e$^-$/Å^2 and $n_{\mathcal{H}_0} = 15$), (b) scattering cross-sections ω^{CS} ($D = 10^5$ e$^-$/Å^2 and $n_{\mathcal{H}_0} = 30$), and (c) images ω^{Im} ($D = 10^5$ e$^-$/Å^2 and $n_{\mathcal{H}_0} = 30$) of a Sr column with a detector collection range of $60 - 100$ mrad and settings of Table 1 which are explained section 3.1.

2.3. Scattering cross-sections (CS)

As a second measure, next to the peak intensities, one can also use scattering cross-sections under both hypotheses. The scattering cross-section values are computed in the following way (Eq. (5)) [49]:

$$\omega^{CS} = \sum_{k=1}^{K} \sum_{l=1}^{L} \omega_{kl} \cdot dx^2 \tag{11}$$

Voronoi cells can be used to define the integration area for the computation of the scattering cross-sections. A Voronoi cell of an atomic column is the cell formed by the perpendicular bisectors of the direct connections to the neighbouring columns. This definition of the scattering cross-sections is used here for simplicity as the scattering cross-section values can directly be calculated from the simulated STEM images in this way, since the positions of the atomic columns are known from the simulation. Generally, a parametric model consisting of Gaussian peaks at the atomic column positions, is used

to describe the pixel intensities of the STEM image [10, 19, 20, 25]. Then, the scattering cross-section corresponds to the volume under the estimated Gaussian peak. These volumes are equivalent to the computed values from the integration of the Voronoi cells. However, the use of the volumes provides some extra advantages, since the parametric model takes into account overlap between neighbouring atomic columns.

The expected scattering cross-section value equals:

$$\mathbb{E}_{\mathcal{H}_i}\left[\omega^{CS}\right] = \sum_{k=1}^{K}\sum_{l=1}^{L} \lambda_{\mathcal{H}_i,kl} \cdot dx^2 = CS_n \tag{12}$$

where $\lambda_{\mathcal{H}_i,kl} = \mathbb{E}_{\mathcal{H}_i}[\omega_{kl}]$ corresponds to the expectation values for the pixel intensities of the STEM image of the atomic column and CS_n is the expected scattering cross-section for n atoms. Since a sum of independent Poisson distributed variables is known to be Poisson distributed [50], the variable

$$\sum_{k=1}^{K}\sum_{l=1}^{L} \omega_{kl} \tag{13}$$

is therefore also Poisson distributed. The expected value $\lambda_{\mathcal{H}_i}$ then equals:

$$\lambda_{\mathcal{H}_i} = \sum_{k=1}^{K}\sum_{l=1}^{L} \lambda_{\mathcal{H}_i,kl}. \tag{14}$$

The conditional probability distribution for a scattering cross-section taking into account the constant factor dx^2, is then given by:

$$p(\omega^{CS};\mathcal{H}_i) = \frac{\left(\lambda_{\mathcal{H}_i}\right)^{\frac{\omega^{CS}}{dx^2}}}{\left(\frac{\omega^{CS}}{dx^2}\right)!} \exp\left(-\lambda_{\mathcal{H}_i}\right), \tag{15}$$

Analogous to the decision rule for the peak intensities of Eq. (8), we decide $\mathcal{H}_1$ for the scattering cross-sections when assuming equal prior probabilities

$P(\mathcal{H}_0) = P(\mathcal{H}_1) = 1/2$ if:

$$p(\omega^{CS}; \mathcal{H}_1) > p(\omega^{CS}; \mathcal{H}_0) \tag{16}$$

otherwise $\mathcal{H}_0$ is decided. This decision rule and the calculation of the probability of error using the conditional probability function given by Eq. (15) is illustrated in Fig. 1(b). The probability of error is then reformulated as follows for the scattering cross-sections:

$$\begin{aligned} P_e =& \frac{1}{2} P(\mathcal{H}_0|\mathcal{H}_1) + \frac{1}{2} P(\mathcal{H}_1|\mathcal{H}_0) \\ =& \frac{1}{2} F\left(\frac{x^{CS}}{dx^2}; \lambda_{\mathcal{H}_1}\right) + \frac{1}{2}\left[1 - F\left(\frac{x^{CS}}{dx^2}; \lambda_{\mathcal{H}_0}\right)\right] \end{aligned} \tag{17}$$

where $F\left(\frac{x^{CS}}{dx^2}; \lambda_{\mathcal{H}_i}\right)$ equals the Poisson cumulative distribution function with parameter $\lambda_{\mathcal{H}_i}$ evaluated at x^{CS}/dx^2 and x^{CS} is the intersection of the two probability functions $p(\omega^{CS}; \mathcal{H}_0)$ and $p(\omega^{CS}; \mathcal{H}_1)$ given by:

$$x^{CS} = \frac{(\lambda_{\mathcal{H}_0} - \lambda_{\mathcal{H}_1})\, dx^2}{\ln \frac{\lambda_{\mathcal{H}_0}}{\lambda_{\mathcal{H}_1}}}. \tag{18}$$

If one now wants to count the number of atoms in a column with single atom sensitivity, the goal is to optimise the experiment design as a function of the detector settings in order to have the lowest probability of choosing the wrong number of atoms. The detector configuration for which the probability of error reaches a minimum is then considered as the optimal detector setting. From Fig. 1(b), it can be seen that the probability of error decreases if the two distributions are more separated. A high difference between the expected values is therefore desired, as well as small values for the width of the distributions. The difference between the expected values of ω^{CS} for each

hypothesis can be expressed as:

$$\mathbb{E}_{\mathcal{H}_1}\left[\omega^{CS}\right] - \mathbb{E}_{\mathcal{H}_0}\left[\omega^{CS}\right] = (CS_n + \Delta CS_{n,n+1}) - CS_n = \Delta CS_{n,n+1} \tag{19}$$

with $\Delta CS_{n,n+1}$ the expected difference in cross-section between two columns having n and $(n+1)$ atoms. The difference in expected values equals $\Delta CS_{n,n+1}$. However, when $\Delta CS_{n,n+1}$ increases, the variances also increase. The variances are calculated from the probability distribution given by Eq. (15) and can be expressed as:

$$\mathrm{var}_{\mathcal{H}_0}\left[\omega^{CS}\right] = CS_n \cdot dx^2 \tag{20}$$

$$\mathrm{var}_{\mathcal{H}_1}\left[\omega^{CS}\right] = (CS_n + \Delta CS_{n,n+1}) \cdot dx^2 \tag{21}$$

Since the width of the distribution is proportional to $\sqrt{CS_n}$ and $\sqrt{CS_n + \Delta CS_{n,n+1}}$ for $\mathcal{H}_0$ and $\mathcal{H}_1$ respectively, the probability of error will become smaller for increasing $\Delta CS_{n,n+1}$, that is when the difference in cross-section between two columns increases.

2.4. STEM images

As a third measure to count the number atoms the STEM images of the atomic column are considered. When assuming that the pixels in a STEM image are statistically independent electron counting results, the conditional joint probability function for a STEM image of an atom column is given by:

$$p(\boldsymbol{\omega}^{Im}; \mathcal{H}_i) = \prod_{k=1}^{K}\prod_{l=1}^{L} \frac{\left(\lambda_{\mathcal{H}_i,kl}\right)^{\omega_{kl}}}{\omega_{kl}!} \exp\left(-\lambda_{\mathcal{H}_i,kl}\right). \tag{22}$$

Since we have a *joint* probability function for the stochastic variable $\boldsymbol{\omega}^{Im}$ of the STEM image of an atomic column, it is not possible to compute the

probability of error directly from the overlapping areas of $p(\boldsymbol{\omega}^{Im};\mathcal{H}_0)$ and $p(\boldsymbol{\omega}^{Im};\mathcal{H}_1)$. However, as shown by Gonnissen et al. [39], it is possible to calculate this probability of error analytically by reformulating the decision rule using the so-called log-likelihood ratio $\ln \mathrm{LR}(\boldsymbol{\omega}^{Im})$. After reformulation of Eq. (3), we then decide $\mathcal{H}_1$ if

$$\ln \mathrm{LR}(\boldsymbol{\omega}^{Im}) \equiv \ln\left(\frac{p(\omega^{Im};\mathcal{H}_1)}{p(\omega^{Im};\mathcal{H}_0)}\right) > \ln(1) = 0, \tag{23}$$

otherwise $\mathcal{H}_0$ is decided, for equal prior probabilities. This corresponds to choosing the hypothesis for which the log-likelihood function is maximal. The function $LR(\omega)$ is called the likelihood ratio since it indicates for each set of observations of ω^{Im} the likelihood of $\mathcal{H}_1$ versus the likelihood of $\mathcal{H}_0$. Given the decision rule of Eq. (23), the expression for the probability of error $\mathrm{P_e}$ given by Eq. (2), can be rewritten as follows:

$$\begin{aligned}\mathrm{P_e} &= \frac{1}{2}P(\mathcal{H}_0|\mathcal{H}_1) + \frac{1}{2}P(\mathcal{H}_1|\mathcal{H}_0) \\ &= \frac{1}{2}P\left(\ln \mathrm{LR}(\omega) < 0|\mathcal{H}_1\right) + \frac{1}{2}P\left(\ln \mathrm{LR}(\omega) > 0|\mathcal{H}_0\right).\end{aligned} \tag{24}$$

When using the conditional joint probability function for STEM images given by Eq. (22), the log-likelihood ratio defined by Eq. (23) can be rewritten as

$$\ln \mathrm{LR}(\boldsymbol{\omega}^{Im}) = \sum_{k=1}^{K}\sum_{l=1}^{L}\left(\omega_{kl}\ln\left(\frac{\lambda_{\mathcal{H}_1,kl}}{\lambda_{\mathcal{H}_0,kl}}\right) - \lambda_{\mathcal{H}_1,kl} + \lambda_{\mathcal{H}_0,kl}\right). \tag{25}$$

Following the central limit theorem, the log-likelihood ratio tends to be normally distributed:

$$p(\ln \mathrm{LR}(\boldsymbol{\omega}^{Im});\mathcal{H}_i) = \frac{1}{\sigma_{\mathcal{H}_i}\sqrt{2\pi}}\exp\left(-\frac{\left(\ln \mathrm{LR}(\boldsymbol{\omega}^{Im}) - \mu_{\mathcal{H}_i}\right)^2}{2{\sigma_{\mathcal{H}_i}}^2}\right) \tag{26}$$

For STEM images the expected value and variance characterising this normal distribution of $\ln \mathrm{LR}(\omega^{Im})$, can be computed from Eq. (25) when assuming $\mathcal{H}_i$ to be true, giving the following results:

$$\begin{aligned}\mu_{\mathcal{H}_i} &= \mathbb{E}_{\mathcal{H}_i}\left[\ln \mathrm{LR}(\boldsymbol{\omega}^{Im})\right] \\ &= \sum_{k=1}^{K}\sum_{l=1}^{L}\left(\lambda_{\mathcal{H}_i,kl}\ln\frac{\lambda_{\mathcal{H}_1,kl}}{\lambda_{\mathcal{H}_0,kl}} - \lambda_{\mathcal{H}_1,kl} + \lambda_{\mathcal{H}_0,kl}\right), \qquad (27)\\ {\sigma_{\mathcal{H}_i}}^2 &= \mathrm{var}_{\mathcal{H}_i}\left[\ln \mathrm{LR}(\boldsymbol{\omega}^{Im})\right] \\ &= \sum_{k=1}^{K}\sum_{l=1}^{L}\lambda_{\mathcal{H}_i,kl}\left(\ln\frac{\lambda_{\mathcal{H}_1,kl}}{\lambda_{\mathcal{H}_0,kl}}\right)^2. \qquad (28)\end{aligned}$$

In this derivation, use is made of the property that the variance of a Poisson distributed variable equals its expectation value, $\mathbb{E}_{\mathcal{H}_i}[\omega_{kl}] = \mathrm{var}_{\mathcal{H}_i}[\omega_{kl}] = \lambda_{\mathcal{H}_i,kl}$. The explicit description of the distribution of the log-likelihood ratio now enables us to unambiguously compute the probability of error given by Eq. (24), resulting in the following general expression:

$$\mathrm{P_e} = \frac{1}{2}\left[\Phi\left(\frac{-\mu_{\mathcal{H}_1}}{\sigma_{\mathcal{H}_1}}\right) + \Phi\left(\frac{\mu_{\mathcal{H}_0}}{\sigma_{\mathcal{H}_0}}\right)\right] \qquad (29)$$

with $\Phi(\pm\mu/\sigma)$ the cumulative distribution function of the standard normal distribution evaluated at $\pm\mu/\sigma$. The meaning of the expected value $\mu_{\mathcal{H}_i}$ and variance ${\sigma_{\mathcal{H}_i}}^2$ characterising the normal distributions of $\ln \mathrm{LR}(\boldsymbol{\omega}^{Im})$ given by Eq. (26) under both hypotheses, is illustrated in Fig. 1(c) based on STEM images for a Sr column consisting of either 30 or 31 atoms. The decision rule is also clarified: $\mathcal{H}_0$ is decided for $\ln \mathrm{LR}(\boldsymbol{\omega}^{Im}) < 0$, otherwise $\mathcal{H}_1$ is decided to be correct. The dark grey region denotes the error which is made if $\mathcal{H}_0$ is chosen while $\mathcal{H}_1$ is correct, and vice versa for the light grey region. It is clear from this figure that the probability of error here also corresponds to the overlap between both distributions.

2.5. Multiple hypothesis test for atom-counting

A binary hypothesis test is no longer adequate if different choices of the two hypotheses lead to different designs. Therefore, the approach of binary hypothesis testing for atom-counting is extended towards multiple hypothesis testing. The multiple hypothesis test will be described for the scattering cross-sections, which are often used in practice [19, 20, 47]. The number of hypotheses in the multiple hypothesis test equals the maximum number of atoms in a column which depends on the sample under study. In this case, we want to differentiate between $1, 2, \ldots, M$ atoms in a projected atomic column and therefore we decide among M possible hypotheses:

$$\{\mathcal{H}_0, \mathcal{H}_1, \ldots, \mathcal{H}_{M-1}\}. \tag{30}$$

In practice, the number of hypotheses that is included for the decision rule, is chosen sufficiently large such that the observed scattering cross-section for sure corresponds to one of the considered hypotheses; M will be typically larger than the unknown thickness of the sample. Equivalent to Eq. (3), the decision rule is now defined such that the probability of error is minimised. The minimum probability of error decision rule is then to decide $\mathcal{H}_k$ if

$$p(\omega^{CS}; \mathcal{H}_k)P(\mathcal{H}_k) > p(\omega^{CS}; \mathcal{H}_i)P(\mathcal{H}_i) \quad \forall i \neq k. \tag{31}$$

For equal prior probabilities $P(\mathcal{H}_i) = 1/M$, which we assume here, we decide $\mathcal{H}_k$ if

$$p(\omega^{CS}; \mathcal{H}_k) > p(\omega^{CS}; \mathcal{H}_i) \quad \forall i \neq k. \tag{32}$$

An illustration of the conditional probability functions of a multiple hypothesis test consisting of $M = 30$ hypotheses is given in Fig. 2. Analogously

to the binary test of section 2.3, the probability of error for the scattering cross-section for a multiple hypothesis test can be calculated from the overlapping areas of the conditional probability functions (weighted by their prior probability):

$$\mathrm{P_e} = \sum_{i=0}^{M-1} \sum_{j=0}^{M-1} C_{ij} P(\mathcal{H}_i|\mathcal{H}_j) P(\mathcal{H}_j), \tag{33}$$

where

$$C_{ij} = \begin{cases} 1 & i \neq j \\ 0 & i = j \end{cases} \tag{34}$$

The number of terms for the calculation of the probability of error of a multiple hypothesis test used in Eq. (33) equals $M(M-1)$. Therefore, it is more efficient to calculate $\mathrm{P_c} = 1 - \mathrm{P_e}$, where $\mathrm{P_c}$ is the probability of a correct decision. In this case, the number of terms in the summation reduces to M:

$$\mathrm{P_c} = \sum_{i=0}^{M-1} P(\mathcal{H}_i|\mathcal{H}_i) P(\mathcal{H}_i) \tag{35}$$

This expression can be calculated analytically for the scattering cross-sections, since their conditional probability functions are well-known from Eq. (15). The probability of a correct decision for equal prior probabilities $P(\mathcal{H}_i) =$

$1/M$ then corresponds to:

$$\begin{aligned} \mathrm{P_c} = \frac{1}{M} \Bigg[& F\left(\frac{x^{CS_{0,1}}}{dx^2}, \lambda_{\mathcal{H}_0^s}\right) + \\ & F\left(\frac{x^{CS_{1,2}}}{dx^2}, \lambda_{\mathcal{H}_1^s}\right) - F\left(\frac{x^{CS_{1,0}}}{dx^2}, \lambda_{\mathcal{H}_1^s}\right) + \\ & F\left(\frac{x^{CS_{2,3}}}{dx^2}, \lambda_{\mathcal{H}_2^s}\right) - F\left(\frac{x^{CS_{2,1}}}{dx^2}, \lambda_{\mathcal{H}_2^s}\right) + \\ & \ldots + \\ & \left(1 - F\left(\frac{x^{CS_{M-1,M-2}}}{dx^2}, \lambda_{\mathcal{H}_{M-1}^s}\right)\right)\Bigg] \end{aligned} \tag{36}$$

where $\mathcal{H}_i^s$ denotes the sorted hypotheses according to the expected values of the scattering cross-sections, $x^{CS_{i,j}} = x^{CS_{j,i}}$ corresponds to the intersection between two neighbouring probability distribution functions which is given by Eq. (18), $\lambda_{\mathcal{H}_i}$ corresponds to Eq. (14), and $F\left(\frac{x^{CS_{i,i}}}{dx^2}, \lambda_{\mathcal{H}_i^s}\right)$ equals the Poisson cumulative distribution function with parameter $\lambda_{\mathcal{H}_i^s}$ evaluated at $x^{CS_{i,i}}/dx^2$. This allows us to calculate analytically the probability of error $\mathrm{P_e}$ for atom-counting. If the decision for a certain hypothesis between M different hypotheses is completely random, the probability for a correct decision equals $1/M$ when assuming equal prior probabilities. Then, it follows that for a multiple hypothesis test with M different hypotheses the maximum value for the probability of error equals $(M-1)/M$.

The optimal experiment design can now be investigated for a realistic simulation experiment, using the analytical expressions for the probability of error for both the binary and the multiple hypothesis test. The obtained results for the proposed measures (peak-intensities, scattering cross-sections, or STEM images) will be compared.

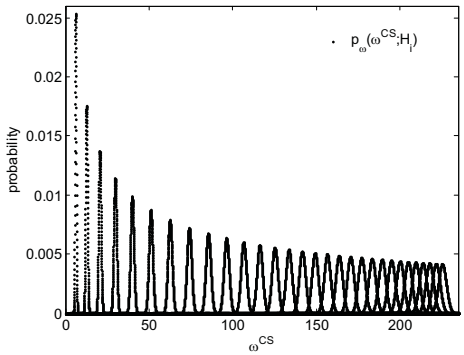

Figure 2: Conditional probability functions for a multiple hypothesis test of $M = 30$ for a Sr column with $D = 10^5$ e$^-$/Å^2, for a detector collection range of $60 - 100$ mrad and settings of Table 1 which are explained in section 3.1.

3. Optimal experiment design

3.1. Simulation experiments

In this section, the results will be presented of a simulation study that has been performed in order to investigate the probability of error defined in Section 2 to evaluate and optimise the inner and outer detector radii of an annular STEM detector in terms of quantitative atom-counting. Simulations of STEM images are performed for a 30 nm thick $SrTiO_3$ crystal, i.e. a thickness of 75 atoms, using the software STEMsim [42], for an aberration-corrected microscope at Scherzer defocus. The multislice approach is used in which thermal diffuse scattering is included as an absorptive potential. The simulation parameters which are used are listed in Table 1.

3.2. Results from binary hypothesis test

In Fig. 3 the results for the probability of error from a binary hypothesis test with equal prior probabilities, defined by Eq. (2) are shown as a function

Parameter	Symbol	Value
Slice thickness	z_{slice} (Å)	1.95
Debye-Waller factor Sr	B (Å^2)	0.6214
Debye-Waller factor Ti	B (Å^2)	0.4398
Debye-Waller factor O	B (Å^2)	0.7323
Acceleration voltage	V (kV)	300
Defocus	ε (Å)	-14.03
Spherical aberration	C_s (mm)	0.001
Spherical aberration of fifth order	C_5 (mm)	0
Semi-convergence angle	α (mrad)	20
Probe sampling distance	dx (Å)	0.1562
FWHM of the source image	$FWHM_s$ (Å)	0.7
Size of the supercell	$N_a \times N_b$ (nm^2)	4.3 × 4.3
Total number of scanned pixels	$K \times L$	25 × 25

Table 1: Parameter values used in the simulation software STEMsim [42].

of the number of atoms $n_{\mathcal{H}_0}$ in a Sr column for the three proposed measures and for two different incident electron doses. The dose only changes the value of the probability of error; for a higher electron dose, the probability of error becomes lower. It can be seen that the probability of error increases for an increasing number of atoms. This means that it is easier to differentiate between two atomic columns containing 1 and 2 atoms than to differentiate between 75 and 76 atoms in a column. Another important conclusion that can be drawn from this figure concerns the different results for the three measures which we consider. The probability of error for the scattering cross-

sections (red dots) using Eq. (17) almost equals the probability of error for the STEM images (blue squares) for which Eq. (29) is used, whereas the probability of error for the peak intensities (green crosses), computed using Eq. (9) is significantly larger. This means that the scattering cross-sections contain almost the same amount of information as the images themselves in terms of atom-counting, provided that the scattering cross-sections monotonically increase with number of atoms. Thus, the detailed profiles of the atomic columns do not add extra information for atom-counting. These differences can only be detected when using the images, since the scattering cross-sections sum all the pixel values in a Voronoi cell in the image into one number defined by Eq. (11). This result is very beneficial since the scattering cross-sections are now often used as a measure to analyse the number of atoms in an atomic column and in addition the scattering cross-sections are far more robust to compare with simulations. Scattering cross-sections are independent of the FWHM of the source size used, the defocus and other parameters [49, 51].

In Fig. 4 the probability of error is shown as a function of the inner detector radius with a fixed outer detector radius of 100 mrad. The incident electron dose is chosen such that the values for the probability of error range between 0 and 0.5. The optimal inner angle is not affected by the selected electron dose. In Fig. 4(a), results for P_e are shown for $n_{\mathcal{H}_0} = 1$ for the three different measures for a Sr column. From this, we can conclude that the optimal inner detector radius equals 21 mrad since the probability of error reaches a minimum here, suggesting that imaging in the LAADF STEM regime is optimal for atom-counting. However, when choosing $n_{\mathcal{H}_0} = 75$, the optimal

inner detector radius increases to 28 mrad, as can be seen in Fig. 4(b). For this value of $n_{\mathcal{H}_0} = 75$, $21 - 100$ mrad can definitely not be considered as an optimum, whereas for $n_{\mathcal{H}_0} = 1$ an inner detector radius of 28 mrad is near-optimal for atom-counting. Because the optimal detector design depends on the choice of hypotheses, we should move on toward multiple hypothesis testing as already suggested in the theory part in section 2.

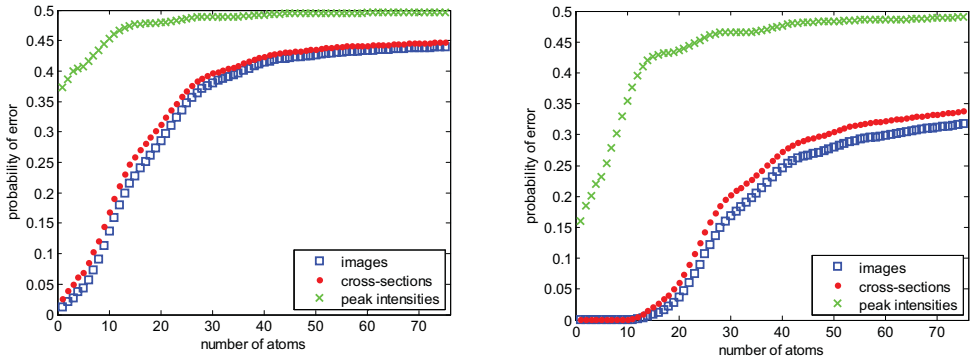

(a) $D = 10^4$ e$^-$/Å^2 (b) $D = 10^5$ e$^-$/Å^2

Figure 3: Probability of error as a function of the number of atoms in a Sr column with $D = 10^5$ e$^-$/Å^2, for a detector collection range of $60 - 100$ mrad using a binary hypothesis test.

3.3. Results from multiple hypothesis test

When using a multiple hypothesis test, all possible numbers of atoms up to a certain thickness of the atom column are considered. Since we demonstrated in section 3.2 that for atom-counting the scattering cross-sections contain almost the same amount of information as the images, we proceed here with the scattering cross-sections, which are often used in practice [20, 20, 25]. It can also be shown that in the case of a multiple hypothesis test the general

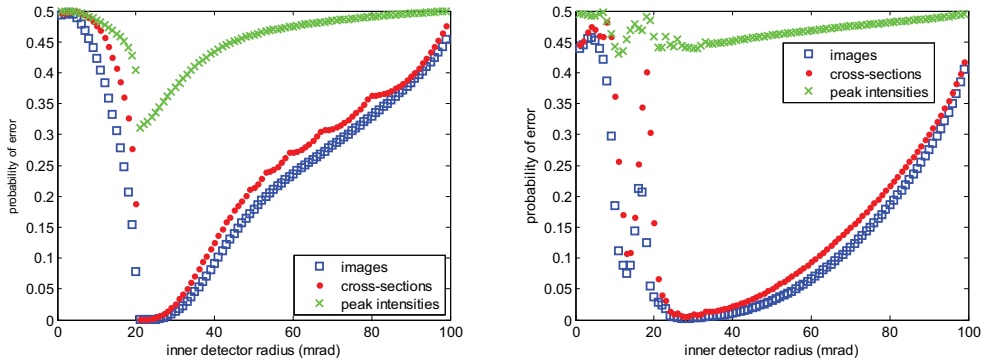

(a) $n_{\mathcal{H}_0} = 1$ and $D = 10^3$ e$^-$/Å^2 (b) $n_{\mathcal{H}_0} = 75$ and $D = 10^6$ e$^-$/Å^2

Figure 4: Probability of error for a Sr column as a function of the inner detector angle with a fixed outer detector radius (100 mrad) using a binary hypothesis test.

optimal detector design does not drastically changes when using STEM images. Using Eq. (36), it is possible to determine the optimal detector design for the STEM detector in terms of inner and outer detector radius. Therefore we calculate the probability of error for the different atomic columns in the $SrTiO_3$ crystal for a multiple hypothesis test with $M = 15$ hypotheses, i.e. for a thickness up to 15 atoms, and for a test with 75 hypotheses, i.e. for a thickness up to $M = 75$ atoms and assuming equal prior probabilities for the different hypotheses. Since the TiO column exists of an equal number of Ti and O atoms, only counting of one type of atoms is considered. The results are shown in Fig. 5 for the scattering cross-sections. The optimal detector angles do not critically depend on the atom type. For a thickness of 15 atoms, the optimal detector design is LAADF STEM with an inner detector radius of 21 mrad and an outer detector radius of 100 mrad. The optimal detector design changes for a thickness of 75 atoms. Here we find a minimum for the probability of error for a Sr column at $28 - 100$ mrad, for

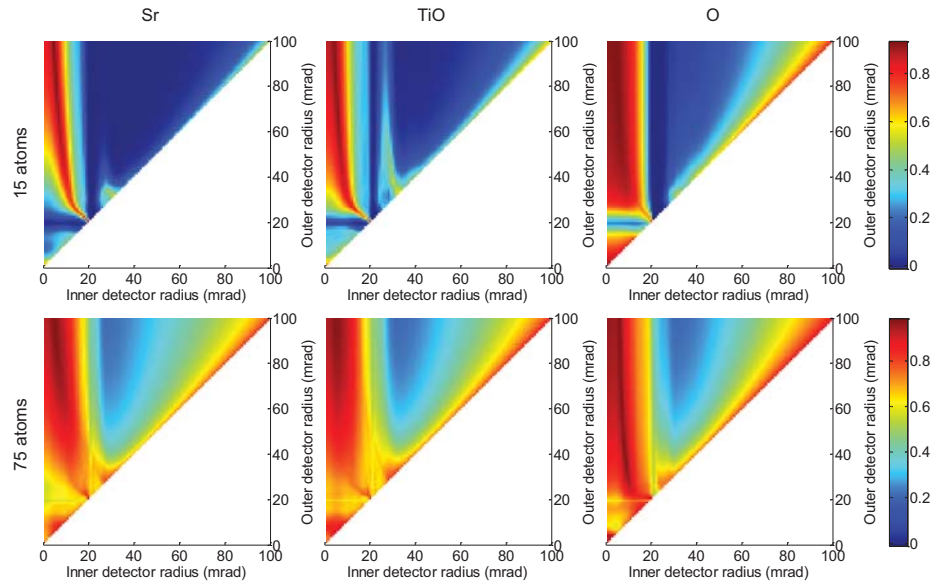

Figure 5: Probability of error for scattering cross-sections as a function of inner and outer detector angle for the three different atom columns in $SrTiO_3$ for $D = 10^5$ $e^-/Å^2$ using a multiple hypothesis test. The upper and lower row show the results when the goal is to find the optimal settings when counting up to $M = 15$ and $M = 75$ atoms, respectively.

a TiO column at $33 - 100$ mrad and for a O column at $30 - 100$ mrad.

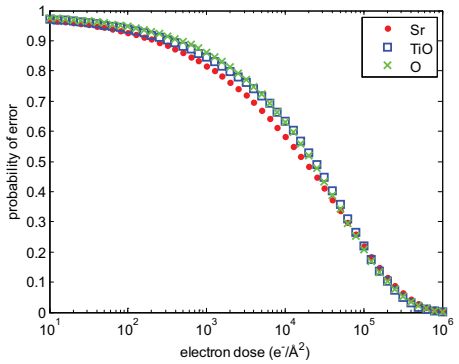

Figure 6: Probability of error as a function of incident electron dose for detector angles $30 - 100$ mrad and thickness of $M = 75$ atoms using a multiple hypothesis test.

The actual numbers of the probability of error not only depend on the choice of the detector but also on the incident electron dose. Once the optimal detector design has been derived, one can then be interested to investigate the lowest possible incident electron dose for which the probability of error reaches an acceptable low value. Therefore the probability of error is computed as a function of the incident electron dose for scattering cross-sections, for the three different atom columns present in $SrTiO_3$. The results are shown in Fig. 6. It is clear from this figure, as one could expect, that the probability of error decreases for an increasing electron dose. If a maximum probability of error of 20% would be taken as acceptable, then an electron dose of 10^5 $e^-/Å^2$ would be necessary. This can be of great importance if one wants to reduce beam damage but at the same time still obtain an acceptable precision to count atoms.

4. Discussion

In order to understand the different obtained optimal designs for the different thicknesses shown in Figs. 4 and 5, the values of the integrated scattering cross-sections are investigated for three different detector designs for a Sr column. In Fig. 7(a) the normalised integrated scattering cross-sections are shown as a function of thickness, i.e. the number of atoms in a Sr column, for three different detector collection ranges. The red dots show the behaviour of the scattering cross-sections for a collection range of $21 - 100$ mrad, the blue squares give the result for a detector collection range of $30 - 100$ mrad, and the green crosses show the result for a detector ranging from 60 to 100 mrad. There is a clear difference in the results for the three detector settings, from

which we can now understand the optimal designs shown in Fig. 5. Up to a thickness of 20 atoms in a Sr column, there is a monotone increase in the values of the integrated scattering cross-sections. However it is clear from the image that for a detector collection range of $21 - 100$ mrad, i.e. LAADF STEM, this increase is much steeper, which means that for this detector setting $\Delta CS_{n,n+1}$ from Eq. (19) is much larger than for the other detector settings shown. For this reason the detection collection area of $21 - 100$ mrad turns out to be the optimal detector design for a Sr column of 15 atoms thick as can seen from the upper left figure of Fig. 5,. For Sr columns thicker than 20 atoms, however, there appears to be a different behaviour in the scattering cross-sections for a detector collection range of $21 - 100$ mrad. The monotone increase is interrupted by a sudden minimum, whereas for a detector ranging from $30 - 100$ mrad and from $60 - 100$ mrad the scattering cross-sections still increase as a function of thickness. This result shows us why for a thickness of 75 atoms in a Sr column, the detector collection range of $30 - 100$ mrad becomes beneficial. Because the increase in scattering cross-sections for $30 - 100$ mrad is steeper compared to the $60 - 100$ mrad, it is clear that this latter will lead to a higher probability of error and therefore does not result into the optimal design as can be seen from the bottom left image in Fig. 5. In a similar way, the obtained optimal detector designs for a TiO and pure O column given in Fig. 5 can be explained.

In order to understand why scattering cross-sections in the LAADF STEM regime no longer increase monotonically with the number of atoms as compared to the MAADF and HAADF regime, we consider the coherent and incoherent contributions to the scattering cross-sections under different com-

binations of inner and outer detector angles. The simulation software STEMsim allows one to save the coherent and incoherent contributions separately. Following [52], both parts are described by different potentials which are normally summed up in order to obtain the complete signal. In Figs. 7(b),(c), and (d), the coherent and incoherent contributions to the scattering cross-sections are separated for the different detector collection ranges of $21 - 100$ mrad, $30 - 100$ mrad, and $60 - 100$ mrad respectively. As can be seen from Fig. 7(b), the coherent contribution to the scattering cross-sections causes the non-monotonic increase. The relative contribution of the coherent part to the scattering cross-section decreases when increasing the inner detector angle as can be seen from Figs. 7(c) and (d). This analysis shows that the optimal detector design can be understood from the values of the scattering cross-sections, i.e. a combination of the coherent and incoherent contributions, as a function of the number of atoms in a projected atomic column.

5. Conclusions

In this paper, we propose to use the principles of detection theory for quantifying the probability of error for atom-counting from HR STEM images. Therefore, binary hypothesis testing as well as multiple hypothesis testing has been worked out for atom-counting. In this way the limits to the precision with which the number of atoms in a projected atomic column can be estimated are studied. The here-described method is put forward as a powerful tool that can be used to optimise the design of an experiment by varying experimental parameters, such as the detector collection range,

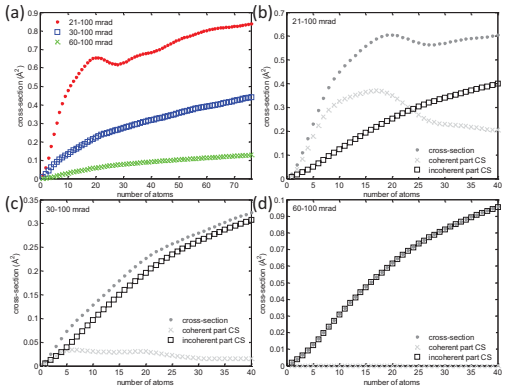

Figure 7: (a) Integrated scattering cross-sections (fraction of incident electron dose) as a function of the number of atoms in a Sr column. The coherent and incoherent contribution to the scattering cross-sections are shown for (b) $21-100$ mrad, (c) $30-100$ mrad, and (d) $60-100$ mrad.

according to the experimental possibilities. Furthermore, the exact optimal experiment design will depend on the material under study. Nevertheless, the conclusions from the study conducted in this paper give some general guidelines on optimal experiment design for atom-counting.

In this paper, it is pointed out that the use of scattering cross-sections, as proposed in [10, 19, 20, 49], is afforded in the quantitative analysis of HR STEM images when the goal is to count the number of atoms as precisely as possible. Scattering cross-sections perform almost equally well as compared to detailed STEM images of a projected atomic column and they even outperform peak intensities. Furthermore, it has been shown that the probability of error increases for increasing number of atoms in the column. In other words, it becomes more difficult to count the number of atoms in a column if the thickness increases. One could also use the proposed method of hypothesis testing to determine the minimally required electron dose in

order to attain a pre-specified precision for the atom-counting. This is very useful when one is working with beam-sensitive materials, so that a minimal electron dose can be predicted in order to attain a pre-specified precision. In this way, beam damage can be kept to a minimum. Finally, it is shown that the optimal inner detector angle increases for increasing thickness when deriving the optimal STEM detector design for atom-counting.

6. Acknowledgements

The authors acknowledge financial support from the Research Foundation Flanders (FWO, Belgium) through project fundings (G.0393.11 and G.0374.13) and a Ph.D. grant to A. De Backer. The research leading to these results has also received funding from the European Union Seventh Framework Programme [FP7/2007-2013] under Grant agreement no. 312483 (ESTEEM2). The authors would like to thank A.J. den Dekker, J. Sijbers and P.D. Nellist for useful discussions and A. Rosenauer for providing access to the STEMsim software.

7. References

[1] H. Rose, Elektronenoptische aplanate, Optik 34 (1971) 285–311.

[2] H. Rose, Outline of a spherically corrected semi-aplanatic medium-voltage transmission electron microscope, Optik 85 (1990) 19–24.

[3] C. L. Jia, S. B. Mi, K. Urban, I. Vrejoiu, M. Alexe, D. Hesse, Atomic-scale study of electric dipoles near charged and uncharged domain walls in ferroelectric films, Nature Materials 7 (2008) 57–61.

[4] K. W. Urban, Studying atomic structures by aberration-corrected transmission electron microscopy, Science 321 (2008) 506.

[5] H. W. Mook, P. Kruit, Optics and design of the fringe field monochromator for a schottky field emission gun, Nuclear Instruments and Methods in Physics Research A 427 (1999) 109–120.

[6] H. Rose, Phase-contrast in scanning transmission electron microscopy, Optik 39(4) (1974) 416.

[7] A. J. den Dekker, S. Van Aert, A. van den Bos, D. Van Dyck, Maximum likelihood estimation of structure parameters from high resolution electron microscopy images. Part I: A theoretical framework, Ultramicroscopy 104 (2005) 83–106.

[8] S. Van Aert, A. J. den Dekker, A. van den Bos, D. Van Dyck, J. H. Chen, Maximum likelihood estimation of structure parameters from high resolution electron microscopy images: Part II: A practical example, Ultramicroscopy 104 (2005) 107–125.

[9] S. Bals, S. Van Aert, G. Van Tendeloo, D. Ávila-Brande, Statistical estimation of atomic positions from exit wave reconstruction with a precision in the picometer range, Physical Review Letters 96 (2006) 096106.

[10] S. Van Aert, J. Verbeeck, R. Erni, S. Bals, M. Luysberg, D. Van Dyck, G. Van Tendeloo, Quantitative atomic resolution mapping using high-angle annular dark field scanning transmission electron microscopy, Ultramicroscopy 109 (2009) 1236–1244.

[11] D. A. Muller, Why changes in bond lengths and cohesion lead to core-level shifts in metals, and consequences for the spatial difference method., Ultramicroscopy 78 (1999) 163–174.

[12] C. Kisielowski, E. Principe, B. Freitag, D. Hubert, Benefits of microscopy with super resolution, Physica B 308-310 (2001) 1090–1096.

[13] R. Enri, H. Heinrich, G. Kostorz, Quantitative characterisation of chemical inhomogeneities in Al-Ag using high-resolution Z-contrast STEM, Ultramicroscopy 94 (2003) 125–133.

[14] J. M. LeBeau, S. D. Findlay, L. J. Allen, S. Stemmer, Standardless atom counting in scanning transmission electron microscopy, Nano Letters 10 (2010) 4405–4408.

[15] J. M. LeBeau, S. D. Findlay, L. J. Allen, S. Stemmer, Quantitative atomic resolution scanning transmission electron microscopy, Physical Review Letters 100 (2008) 206101.

[16] J. M. LeBeau, S. Stemmer, Experimental quantification of annular dark-field images in scanning transmission electron microscopy, Ultramicroscopy 108 (2008) 1653–1658.

[17] J. M. LeBeau, A. J. Alfonso, S. D. Findlay, S. Stemmer, L. J. Allen, Quantitative comparisons of contrast in experimental and simulated bright-field scanning transmission electron microscopy images, Physical Review B 80 (2009) 174106.

[18] J. M. LeBeau, S. D. Findlay, X. Wang, A. J. Jacobson, L. J. Allen,

S. Stemmer, High-angle scattering of fast electrons from crystals containing heavy elements: simulation and experiment, Physical Review B 79 (2010) 214110.

[19] S. Van Aert, A. De Backer, G. T. Martinez, B. Goris, S. Bals, G. Van Tendeloo, A. Rosenauer, Procedure to count atoms with trustworthy single-atom sensitivity, Physical Review B 87 (2013) 064107.

[20] S. Van Aert, K. J. Batenburg, M. D. Rossell, R. Erni, G. Van Tendeloo, Three-dimensional atomic imaging of crystalline nanoparticles, Nature 470 (2011) 374–377.

[21] S. Bals, M. Casavola, M. A. van Huis, S. Van Aert, K. J. Batenburg, G. Van Tendeloo, D. Vanmaekelbergh, Three-dimensional atomic imaging of colloidal core-shell nanocrystals, Nano Letters 11 (8) (2011) 3420–3424.

[22] S. Bals, S. Van Aert, C. P. Romero, K. Lauwaet, M. J. Van Bael, B. Schoeters, B. Partoens, E. Yücelen, P. Lievens, G. Van Tendeloo, Atomic scale dynamics of ultrasmall germanium clusters, Nature Communications 3 (2012) 897.

[23] K. J. Batenburg, A network flow algorithm for reconstructing binary images from discrete x-rays, Journal of Mathematical Imaging and Vision 27 (2007) 175–191.

[24] J. R. Jinschek, K. J. Batenburg, H. A. Calderon, R. Kilaas, V. Radmilovic, C. Kisielowski, 3-D reconstruction of the atomic positions in a simulated gold nanocrystal based on discrete tomography: prospects

of atomic resolution electron tomography, Ultramicroscopy 108 (2008) 589–604.

[25] A. De Backer, G. T. Martinez, A. Rosenauer, S. Van Aert, Atom counting in HAADF STEM using a statistical model-based approach: Methodology, possibilities, and inherent limitations, Ultramicroscopy 134 (2013) 23–33.

[26] E. Bettens, D. Van Dyck, A. J. den Dekker, J. Sijbers, A. van den Bos, Model-based two-object resolution from observations having counting statistics, Ultramicroscopy 77 (1999) 37–48.

[27] A. J. den Dekker, J. Sijbers, V. Van Dyck, How to optimize the design of a quantitative HREM experiment so as to attain the highest precision?, Journal of Microscopy 194 (1999) 95–104.

[28] S. Van Aert, D. Van Dyck, Do smaller probes in a STEM result in more precise measurement of the distances between atom columns?, Philosophical Magazine B 81 (2001) 1833–1846.

[29] A. J. den Dekker, S. Van Aert, D. Van Dyck, A. van den Bos, P. Geuens, Does a monochromator improve the precision in quantitative HRTEM?, Ultramicroscopy 89 (2001) 275–290.

[30] S. Van Aert, A. J. den Dekker, D. Van Dyck, A. van den Bos, High-resolution electron microscopy and electron tomography: resolution versus precision, Journal of Structural Biology 138 (2002) 21–33.

[31] S. Van Aert, A. J. den Dekker, A. van den Bos, D. Van Dyck, High-resolution electron microscopy: From imaging toward measuring, IEEE

Transactions on Instrumentation and Measurement 51 (4) (2002) 611–615.

[32] S. Van Aert, A. J. den Dekker, D. Van Dyck, How to optimize the experimental design of quantitative atomic resolution TEM experiments?, Micron 35 (2004) 425–429.

[33] S. Van Aert, A. J. den Dekker, A. van den Bos, D. Van Dyck, Statistical experimental design for quantitative atomic resolution transmission electron microscopy, Vol. 130 of Advances in Imaging and Electron Physics, Elsevier, 2004, pp. 1 – 164.

[34] W. Van den Broek, S. Van Aert, P. Goos, D. Van Dyck, Throughput maximization of particle radius measurements through balancing size versus current of the electron probe, Ultramicroscopy 111 (2011) 940–947.

[35] A. De Backer, S. Van Aert, D. Van Dyck, High precision measurements of atom column positions using model-based exit wave reconstruction, Ultramicroscopy 111 (2011) 1475–1482.

[36] A. J. den Dekker, J. Gonnissen, A. De Backer, J. Sijbers, S. Van Aert, Estimation of unknown structure parameters from high-resolution STEM images: What are the limits?, Ultramicroscopy 134 (2013) 34–43.

[37] A. Wang, S. Van Aert, P. Goos, D. Van Dyck, Precision of three-dimensional atomic scale measurements from {HRTEM} images: What are the limits?, Ultramicroscopy 114 (2012) 20 – 30.

[38] S. Van Aert, W. Van den Broek, P. Goos, D. Van Dyck, Model-based electron microscopy: From images toward precise numbers for unknown structure parameters, Micron 43 (4) (2012) 509 – 515.

[39] J. Gonnissen, A. De Backer, A. J. den Dekker, G. T. Martinez, A. Rosenauer, J. Sijbers, S. Van Aert, Optimal experimental design for the detection of light atoms from high-resolution scanning transmission electron microscopy images, Applied Physics Letters 105 (063116).

[40] A. Rosenauer, K. Gries, K. Müller, A. Pretorius, M. Schowalter, A. Avramescu, K. Engl, S. Lutgen, Measurement of specimen thickness and composition in $Al_xGa_{1-x}N/GaN$ using high-angle annular dark field images, Ultramicroscopy 109 (2009) 1171–1182.

[41] T. Grieb, K. Müller, O. Rubel, R. Fritz, C. Gloistein, M. Schowalter, N. Neugebohrn, N. Knaub, K. Volz, A. Rosenauer, Determination of the chemical composition of GaNAs using {STEM} {HAADF} imaging and {STEM} strain state analysis, Ultramicroscopy 117 (2012) 15–23.

[42] A. Rosenauer, M. Schowalter, Stemsim - a new software tool for simulation of STEM HAADF Z-contrast imaging, in: A. G. Cullis, P. A. Midgley (Eds.), Microscopy of Semiconducting Materials 2007, Vol. 120 of Springer Proceedings in Physics, Springer Netherlands, 2008, pp. 170–172.

[43] S. J. Pennycook, L. A. Boatner, Chemically sensitive structure-imaging with a scanning transmission electron microscope, Nature 336 (1988) 565–567.

[44] P. Hartel, D. Rose, C. Dinges, Conditions and reasons for incoherent imaging in STEM, Ultramicroscopy 63 (1996) 63–114.

[45] A. Singhal, J. C. Yang, J. M. Gibson, STEM-based mass spectroscopy of supported Re clusters, Ultramicroscopy 67 (1997) 191–206.

[46] P. Voyles, D. A. Muller, J. L. Grazul, P. H. Citrin, H.-J. L. Gossmann, Atomic-scale imaging of individual dopant atoms and clusters in highly n-type bulk Si, Nature 416 (2002) 826–829.

[47] A. De Backer, G. T. Martinez, K. E. MacArthur, L. Jones, A. Béché, P. D. Nellist, S. Van Aert, Dose limited reliability of quantitative annular dark field scanning transmission electron microscopy for nano-particle atom-counting, Ultramicroscopy, submitted-Doi: 10.1016/j.ultramic.2014.11.028.

[48] S. M. Kay, Fundamentals of Statistical Signal Processing. Volume II Detection Theory, Prentice-Hall, Inc., New Jersey, 2009.

[49] H. E, K. E. MacArthur, T. J. Pennycook, E. Okunishi, A. J. D'Alfonso, N. R. Lugg, L. J. Allen, P. D. Nellist, Probe integrated scattering cross sections in the analysis of atomic resolution HAADF STEM images, Ultramicroscopy 133 (2013) 109–119.

[50] A. M. Mood, F. A. Graybill, D. C. Boes, Introduction to the Theory of Statistics, 3rd Edition, McGraw-Hill Book Company, 1974.

[51] G. T. Martinez, A. De Backer, A. Rosenauer, J. Verbeeck, S. Van Aert, The effect of probe inaccuracies on the quantitative model-based anal-

ysis of high angle annular dark field scanning transmission electron microscopy images, Micron 63 (2014) 57–63.

[52] K. Ishizuka, A practical approach for stem image simulation based on the fft multislice method, Ultramicroscopy 90 (2002) 71–83.